Crystal structure-controlled synthesis of $NiMoO_4$/NiO hierarchical microspheres for high-performance supercapacitor and photocatalyst

Kuen-Chan Lee,[a,b] Jen-Hsien Huang,[c] Yen-Ju Wu,[d] Kuan-Syun Wang,[e] Er-Chieh Cho,*[f]

Shih-Chieh Hsu,*[g] and Ting-Yu Liu[e,h,i]

[a]Department of Science Education, National Taipei University of Education, No. 134, Sec. 2, Heping E. Road, Da-an District, Taipei City 106, Taiwan

[b]PhD Program for Neural Regenerative Medicine, College of Medical Science and Technology, Taipei Medical University, 250 Wuxing Street, Taipei City, 110, Taiwan

[c]Department of Green Material Technology, Green Technology Research Institute, CPC Corporation, No.2, Zuonan Rd., Nanzi District, Kaohsiung City, 81126, Taiwan

[d]Center for Basic Research on Materials, National Institute for Materials Science (NIMS), 1-2-1 Sengen, Tsukuba, Ibaraki 305-0047, Japan

[e]Department of Materials Engineering, Ming Chi University of Technology, New Taipei City 243303, Taiwan

[f]Department of Clinical Pharmacy, School of Pharmacy, College of Pharmacy, Taipei Medical University, 250 Wuxing Street, Taipei City, 110, Taiwan

[g]Department of Chemical and Materials Engineering, Tamkang University, No. 151, Yingzhuan Road, Tamsui District, New Taipei City, 25137, Taiwan

[h]Department of Chemical Engineering and Materials Science, Yuan Ze University, Taoyuan City 32003, Taiwan

[i]College of Engineering & Center for Sustainability and Energy Technologies, Chang Gung University, Taoyuan 33302, Taiwan

[f,]*Corresponding author. E-mail: echo@tmu.edu.tw (E. C. Cho) Tel.: +886-2-27361661#6179

[g,]*Corresponding author. E-mail: 137422@o365.tku.edu.tw (S. C. Hsu) Tel: +886-2-26215656#2032

[e,h,i]*Corresponding author. E-mail: tyliu0322@gmail.com (T.Y. Liu) Tel.: +886-2-29089899#6321

Nowadays, worldwide environmental challenges and energy crises are driving researchers to develop multifunctional and highly efficient nanomaterials. In this scenario, the current study reports a dual-functional $NiMoO_4$ (NMO)/NiO hierarchical microsphere prepared using a microwave-assisted hydrothermal method, which serves as a supercapacitor and photocatalyst. The content of α-phase and β-phase of NMO can be regulated by controlling the post annealing temperature and the pH value of precursor solution. The as-prepared NMO/NiO nanocomposites can offer dual Faradaic redox reactions attributed from NMO and NiO leading to remarkable supercapacitor performance. In addition, the constructed heterojunction between NMO and NiO also improves the charger separation leading to excellent photocatalytic capability. Based on our results, the NMO with higher content of β-phase shows a better supercapacitive and photocatalytic performances due to its higher conductivity. The optimal NMO/NiO composite displays a specific capacitance of 943 F/g at 1 A/g and an great cycling stability with 83.1% retention at 5 A/g after 4000 cycles. Additionally, it demonstrates outstanding photocatalytic capability towards the degradation of methylene blue (MB), achieving a rate constant of ($0.0113\ min^{-1}$).

Keyword: $NiMoO_4$/NiO, Heterojunction, Supercapacitor, Asymmetric devices, Photocatalyst

1. Introduction

The swift expansion of the global population and rapid industrialization has resulted in a significant upsurge in environmental pollution, coupled with the looming threat of an energy crisis. Consequently, development of sustainable energy solutions and the adoption of green environmental practices has become urgent and inevitable. In this scenario, the global challenges of environmental and energy crises are driving researchers to develop nanomaterials that possess multi-functional capabilities with high efficiency. Extensive research endeavors have been dedicated to the synthesis of versatile nanomaterials, meticulously designed with tailored properties to suit specific applications. Transition metal oxides (TMOs) have been considered as promising materials for a range of applications, including energy conversion/storage, catalysis, and sensors. This is predominantly attributed to their outstanding electrochemical properties and effective charge transfer capabilities.

Ternary metal molybdates with a typical formula of $AMoO_4$ (A=Ca [1], Ba [2], Mg [3], Fe [4], Zn [5], Cu [6], Mn [7], Co [8], Ni [9]) have attracted much interest in the past decade. Among them, $NiMoO_4$ (NMO) is known for its high catalytic activity, and it is commonly used as a catalyst in hydrodesulfurization processes in the petroleum refining industry [10]. NMO possesses large specific capacitance mainly from the high electrochemical activity of Ni ion (Ni^{2+}/Ni^{4+}) and the Mo ions also can improve the electronic properties [11]. These features make it a promising material for energy storage applications. Moreover, NMO with moderate energy band gap (~2.4 eV) and suitable energy band position has been considered as an emerging visible-light-driven photocatalyst for CO_2 conversion [12] and degradation of organic pollutants [13]. Unfortunately, the low electrical conductivity of NMO poses a hindrance to its electrochemical properties, particularly under high current densities, thus limiting its potential for application in next-generation supercapacitors. Additionally, the photocatalytic activity of NMO is dramatically limited by its rapid electron-hole recombination, even though it possesses a low bandgap suitable for utilizing visible light from the solar spectrum. To tackle these aforementioned issues, numerous efforts have concentrated on constructing heterojunction structures by coupling NMO with other semiconductors [14-16]. In supercapacitive applications, the heterojunction structure formed with binary semiconductors can enhance its energy storage performance, attributed to the presence of multiple oxidation states [17, 18]. Furthermore, heterojunction composites with matching energy level structure can also prevent electron-hole recombination, thereby enhancing photocatalytic capability [19, 20].

Based on the structural arrangement, two phases, usually designated as α-form and β-form, are known of NMO. The α-NMO is low temperature stable phase and the β-NMO remains stable at relatively high temperature. Both α-NMO and β-NMO are monoclinic structure with space group C2/m [21]. The primary difference between them lies in the coordination of the Mo^{6+} ions. In α-NMO, the arrangement involves Mo^{6+} ions coordinating with oxygen atoms, forming an octahedral symmetry. In β-NMO, however, the Mo^{6+} ions are connected in a distorted tetrahedral configuration. It is believed that the physicochemical and electrochemical properties of NMO are highly dependent on the nature of polymorph. For example, the catalytic property of β-NMO is nearly twice as selective for the dehydrogenation of propane to propene compared to α-NMO [22]. However, to the best of our knowledge, the effect of the phase compositions of NMO on the supercapacitive and photocatalytic performance remains unreported until now. In this study, we have constructed heteroarchitectures of NMO with NiO via microwave-assisted hydrothermal method. The resultant NMO/NiO hierarchical microspheres with homogeneous porosity and abundant active sites can reduce the ion transport distance and provide more interfacial area for Faradaic and photocatalytic reactions. The electrochemical properties of the constructed NMO/NiO heterostructures can be boosted due to the multiple oxidation states. Moreover, the internal electric field built at NMO/NiO heterointerfaces also accelerates the separation of photo-induced electrons and holes, leading to improved photocatalytic performance. What's more, in this study, the content of the α-phase and β-phase in the NMO was regulated by altering the annealing temperature and pH value of the precursor solutions. The impact of the phase compositions of NMO on both supercapacitive and photocatalytic performance was also examined.

2. Experimental Section

2.1 Material synthesis

In this study, the NMO/NiO composites were prepared by microwave-assisted hydrothermal method. In a typical procedure, 1.044 g of $Ni(NO_3)_2·6H_2O$ and 0.872 g of $Na_2MoO_4·2H_2O$ were dissolved in 120 mL of de-ionized water (solution A). Then, 0.96 g of urea was dissolved in 40 mL of de-ionized water in another beaker (solution B). Solution B was slowly added into solution A under continuous stirring. The pH value of the mixed precursor solution was adjusted with a certain amount of 1 M HNO_3 and 1 M NaOH to pH=3, 5, 7, 9 and 11. The mixed precursor solution was transferred into a microwave-assisted hydrothermal reactor and kept at 180 ^oC for 2 h. The products were washed with de-ionized water for five times and dried at 80 ^oC. Consequently, the obtained samples were thermal annealed at temperature ranged between 400~700 ^oC. The as-prepared samples were labeled as

NMO/NiO-3 (pH=3), NMO/NiO-5 (pH=5), NMO/NiO-7 (pH=7), NMO/NiO-9 (pH=9) and NMO/NiO-11 (pH=11), respectively.

2.2 Material Characterization

All detail information for the material characterization, evaluation of photocatalytic performance and electrochemical measurements are provided in the Supporting Information.

3. Results and Discussion

3.1 The effect of the annealing temperature

Fig. 1a shows the XRD patterns of the as-prepared samples at different annealing temperatures ranged between 400 and 700 °C (Here, the pH value of precursor solution is fixed at 7). The sample annealing at 400 °C shows two XRD peaks at $2\theta = 36.9$ and 43.4°, corresponding to the (111) and (200) planes of the NiO. The broad bump located between 20 and 30° is probably resulted from the amorphous materials containing unreacted molybdenum-containing compounds. It is clear that the NMO only can be obtained at a thermal annealing temperature higher than 400 °C. As the annealing temperature increases, the proportion of the β-phase also increases, indicating the β-NMO is high temperature stable phase. Additionally, the resulting product comprises both NMO and NiO crystalline phases, when the annealing temperature ranges between 500 and 600°C. By further increasing the temperature to 700 °C, all of the NiO can react with molybdenum-containing compounds to form pure NMO phase, resulting in the exclusive production of β-NMO. The TGA and correspond DSC profiles of the sample are presented in Fig. 1b. It can be observed that there are two stages of weight loss within the temperature range from 30 to 200 °C and from 200 to 420 °C as shown in TGA profile. In addition, the DSC curve also show two broad exothermic peaks at around 80 and 350 °C. The initial weight loss of approximately 6.3% corresponds to the elimination of structural intercalated water molecules, while the subsequent weight loss of approximately 9.6% corresponds to the thermal decomposition of metal hydrate compounds [23]. The functional groups present in these samples were detected by FTIR analysis. As shown in Fig. 1c, the peaks observed at 823 cm^{-1} is attributed to the Ni-O bond in NiO phase [24]. The peaks at 958 and 638 cm^{-1} correspond to the vibrations of MoO_4 tetrahedron existing in NMO [25]. The broad peak appeared at 3450 cm^{-1} can be associated with the −OH stretching band from water molecules [25]. The peaks at 1635 and 1350 cm^{-1} originate from the adsorbed water molecules and the residual nitrate groups [26]. The structural arrangement of these samples was characterized using Raman spectroscopy as displayed in Fig. 1d. It can be observed that the Raman intensity increase with higher annealing temperature, suggesting that thermal treatment results an increased ordered state. The Raman spectrum of the sample annealed at 700 ^{o}C reveals intense bands at 958 and 704 cm^{-1} are associated with the symmetric stretching of the Mo−O and Ni−O−Mo bonds, respectively [26]. The bands at 911 and 886 cm^{-1} are attributed from the asymmetric stretching modes of O–Mo–O bond [26, 27], whereas the bands observed at 895 and 825 cm^{-1} are belonged to the asymmetric modes of MoO_4 ions stretching [28]. The other bands located between 325 and 420 cm^{-1} correspond to the bending mode of O−Mo−O bond [29]. Fig. 1e presents the N_2 adsorption/desorption isotherms for the as-prepared samples annealed at different temperatures. The specific surface area evaluated by BET method were calculated to be 291.3, 182.9, 70.5 and 29.3 m^2/g for the samples annealed from low to high temperatures. Furthermore, the presence of a hysteresis loop in the isotherms generally implies the existence of mesopores, which can be further confirmed by the pore-size distribution of these samples, as shown in Figure 1f. It can be observed that the pore-size distribution becomes broader, with a larger average pore size, at higher annealing temperatures.

The morphological investigation of the samples annealed at different temperatures was performed using SEM and TEM. The sample annealed at 400°C exhibits a 3D flower-like hierarchical morphology with a mean particle size of approximately 1.5 μm, as depicted in Fig. 2a and c. The flower-like structure is composed of numerous interconnected nanoflakes, creating a porous surface. Furthermore, TEM analysis, as depicted in Fig. 2b, reveals that the as-prepared sample possesses a solid interior structure with a porous exterior nanostructure. Based on the TEM image with high magnification (Fig. 2d), the thickness of these nanoflakes can be estimated to be around 2–3 nm. As the annealing temperature is raised from 400 to 600°C, both SEM and TEM images show that the flow-like structure with porous morphology can be maintained without significant damage (Fig. 2a–h). The unique structure can offer large active sites with great penetration capacity, which is favorable for the supercapacitor and photocatalyst applications. However, as the annealing temperature is increased to 700°C, the 3D hierarchical structure collapses, and the nanoflakes are sintered, forming large aggregations as shown in Fig. 2i. Additionally, through TEM observation as illustrated in Fig. 2j, it is evident that the nanoflakes convert into nanoparticles during high-temperature treatment.

The information related to the chemical compositions and valence states of the NMO annealed at 600 ºC were investigated by XPS and the results are displayed in Fig. 3. As illustrated in Fig. 3a, the XPS survey spectrum of NMO annealed at 600 ºC shows convincing existence Ni 2p, Mo 3d, O 1s, C 1s. The Ni 2p spectrum as shown in Fig. 3b can be well fitted into four peaks. The major peaks located at binding energy peaks at 872.8 and 855.2 eV are consistent with the Ni 2p1/2 and Ni 2p3/2 and the minor peaks at 879.1 and 861.0 eV are belonged to the corresponding satellite signal. Furthermore, the two peaks observed from the Mo 3d spectrum in Fig. 3c belong to Mo 3d5/2 and Mo 3d3/2. The two peaks centered at 231.3 and 234.4 eV with an energy difference of 3.1 eV, indicating the presence of Mo^{6+} oxidation state [30]. The O 1s spectrum as shown in Fig. 3d can be de-convoluted into three components at 529.7, 531.1 and 532.7 eV, which are characteristic of M–O–M bond, M–OH bond (M denoted Ni or Mo), and the physically adsorbed H–O–H, respectively [31, 32].

The electrochemical properties of these samples annealed at different temperatures are studied by CV measurement. The CV profiles were recorded in a three-electrode configuration with 1.0 M KOH as electrolyte. All the CV profiles reveal a strong redox peaks suggesting their capacitance characteristics are governed by Faradaic reaction as shown in Fig. 4a. As the annealing temperature increases from 400 to 600 ºC, the enclosed area in the CV loop gradually expands, suggesting the enhanced electrochemical activity and capacitance. The large CV response can be attributed to the formation of binary phase (NMO/NiO), which can provide the dual Faradaic redox reactions of Ni^{2+}/Ni^{3+} and the insertion/ extraction of OH^- anions in NiO as follows [30]:

NiMoO4: $\mathrm{NiMoO_4 \leftrightarrow Ni^{2+} + MoO_4^{2-}}$

$$\mathrm{Ni^{2+} + 2OH^- \leftrightarrow Ni(OH)_2}$$

$$\mathrm{Ni(OH)_2 + OH^- \leftrightarrow NiOOH + H_2O + e^-}$$

NiO: $\mathrm{NiO + OH^- \leftrightarrow NiOOH + e^-}$

Nevertheless, the enclosed area in the CV noticeably decreases again as the annealing temperature is further raised to 700 °C. The results likely stems from the unfavorable morphology depicted in Fig. 2i and j. The electrochemical polarization of the four samples, as determined by the potential difference between the anodic and cathodic peaks, is illustrated in Fig. 4b. The CV profiles of the four samples with various scan rates are provided in Fig. S1. The electrochemical polarization decreases from 0.215 V for NiO (400 °C) to 0.112 V for NMO/NiO (600 °C) and finally increases to 0.141 V for NMO/NiO (700 °C). The significant polarization of NiO (400 °C) is likely due to the presence of unreacted molybdenum-containing materials, which cannot contribute to electrochemical activity leading higher resistance. Moreover, it has been observed that the electrical conductivity of β-NMO is significantly higher than that of α-NMO [33, 34]. Hence, the reduced polarization of NMO/NiO (600 °C) compared to NMO/NiO (500 °C) is attributed to its higher proportion of the β-phase. However, the sample annealed at 700 °C loses its flow-like nanomorphology, instead forming large aggregations. Consequently, its polarization increases once more due to the unfavorable morphology. The EIS results of the four samples are also presented in Fig. 4c. Based on the results, the charge transfer resistance (Rct) of these samples annealed at 400, 500, 600 and 700 °C is evaluated to be 8.78, 5.21, 4.55 and 6.69 Ω, respectively, a trend consistent with the polarization results depicted in Fig. 4b. The galvanostatic charge/discharge (GCD) profiles of these samples are presented in Fig. 4d. Consistent with the CV profiles, the NMO/NiO (600 °C) exhibits the longest discharge profile, suggesting the highest specific capacitance. Based on the GCD profiles tested at 1 A/g, the specific capacitance of the samples annealed from 400 to 700 °C is calculated to be 482.3, 631.5, 802.0 and 594.4 F/g, respectively. The capacitance of these samples at various current densities ranging from 1 to 6 A/g is also evaluated as shown in Fig. 4e. Clearly, the NMO/NiO (600 °C) demonstrates a higher capacitance with better rate capability, with values of 802.0, 758.3, 728.1, 695.3, 665.5, and 634.2 F/g at 1, 2, 3, 4, 5, and 6 A/g, respectively. The GCD profiles of NMO/NiO (600 ^{o}C) collected at different current densities are shown in Fig. 4f. The results for the other three samples are also provided in Fig. S2. The better electrochemical performance of NMO/NiO (600 ^{o}C) can be attributed to the synergistic effect of the binary NMO/NiO composition and larger content of β-phase NMO (higher conductive phase than that of α-phase).

3.2 The effect of the precursor solution's pH value

The above results confirm that the optimal annealing temperature for achieving the best electrochemical performance is 600 ^{o}C. Next, we modulate the pH value of the precursor solutions with a fixed annealing temperature at 600 ^{o}C to prepare high-performance NMO. By changing the pH value of the precursor solution, the NMO/NiO composites with different content of α- and β-NMO phase can be obtained as shown in Fig. 5a. It can be observed that the NMO prepared from pH=3 reveal only α-phase. With the pH value rising from pH=3 (NMO/NiO-3) to pH=9 (NMO/NiO-9), the proportion of the β-NMO phase within the NMO steadily rises. Remarkably, the sample derived from pH=9 exclusively exhibits β-NMO. These results suggest that the formation of the β-phase is facilitated by both high annealing temperatures and alkaline conditions. However, when the pH value of precursor solution is further increased to 11, the resulting product unexpectedly exhibits the NiO phase without the formation of NMO. It has been noted that the presence of excess hydroxide ions in the precursor solutions under highly alkaline conditions results in the formation of $Ni(OH)_2$ particles, $Ni^{2+} + 2OH^{-} \rightarrow Ni(OH)_2$. In contrast, MoO_4^{2-} ions scarcely undergo any reaction, and Mo elements persist in an amorphous state within the nanomaterials [35]. Consequently, these $Ni(OH)_2$ particles convert into NiO after the thermal annealing. The morphological evolution of the NMO/NiO composite at different pH values is also monitored by SEM as shown in Fig. 5b-f. As the pH value increases, the morphologies of NMO/NiO composites undergo a transformation. At pH=3, the as-prepared NMO/NiO-3 presents as stacked nanosheets, converting into a flower-like structure between pH=5 and pH=9, and eventually forming aggregated nanoparticles at pH=11 (NMO/NiO-11). It is noteworthy that the morphology of NMO/NiO-

9 displays a more well-defined flower-like structure with a more uniform open porosity compared to NMO/NiO-5 and NMO/NiO-7. It is believed that the 3D nanoarchitecture featuring highly interconnected wavy nanoflakes can offer a large accessible surface area and improved diffusion pathways for OH^- ions, resulting in rapid kinetics and high capacitance

The CV profiles of these samples are shown in Fig. 6a to study the effect of precursor solution's pH value on the electrochemical properties. The rise in CV area as pH increases from 3 to 9 further supports the idea that β-NMO enhances electrochemical activity because of its superior conductivity compared to α-NMO. [33, 34]. Fig. 6b also presents the relationship between peak current (i) and the square root ($\upsilon^{1/2}$) of the scan rate, derived from the CV profiles, to investigate the electrochemical kinetics of these samples. All the i–$\upsilon^{1/2}$ plots exhibit linear behavior, indicating an ionic diffusion-controlled mechanism in the redox reaction. Moreover, it is evident that the NMO/NiO-9 displays the largest slope among these samples, implying its highest electrochemical kinetics based on the Randles–Ševčík relationship [36]. The CV profiles of NMO/NiO-9 hierarchical microsphere with different scan rates are presented in Fig. 6c. The CV profiles of other samples are provided in Fig. S3. The specific capacitance of the five samples as a function of current density is plotted in Fig. 6d. The specific capacitance at 1 A/g is calculated to be 542, 763, 802, 943 and 385 F/g for the samples obtained at pH=3, 5, 7, 9 and 11, respectively. The variation in capacitance with pH value for these samples aligns with the CV results depicted in Fig. 6a. Furthermore, NMO/NiO-9 demonstrates an 83.2% capacitance retention (compared to the value at 1 A/g) at 6 A/g, which is higher than the other samples, suggesting its outstanding rate capability. The corresponding GCD profiles of NMO/NiO-9 are displayed in Fig. 6e and the results for the other samples are shown in Fig. S4. Fig. 6f shows the cycling stability of NMO/NiO-9 tested at 5 A/g for 4000 cycles. After 4000 cycles, the NMO/NiO-9 electrode still can deliver a capacitance of 677.3 F/g with a 16.9% loss to the initial value. The great electrochemical properties can be attributed to its unique nanoarchitecture and the multiple Faradaic redox from the binary composite (NMO/NiO).

Through optimization of annealing temperature and pH value, the NMO/NiO-9 hierarchical microsphere demonstrates superior electrochemical performance, exhibiting large capacitance, remarkable rate capability, and reversibility. To further assess the practical applicability of NMO/NiO-9, an asymmetric supercapacitor cell was assembled using NMO/NiO-9 as the cathode and activated carbon (AC) as the anode. To achieve optimal performance of the NMO/NiO-9//AC device, the mass ratio of cathode to anode was maintained at approximately 1:3.27, ensuring charge balance between the two electrodes (refer to Fig. S5). The CV profiles of the NMO/NiO-9//AC device with different operation windows at a scan rate of 100 mV/s are shown in Fig. 7a. When the working voltage exceeded 1.5 V, an undesired peak attributed to oxygen evolution can be observed in the CV profile. Furthermore, the ratio of the anodic to cathodic area (Qa/Qc) calculated from the CV loop with different operation voltages is also presented in Fig. 7b. With an operation window larger than 1.5 V, the Qa/Qc ratio dramatically increases, indicating the occurrence of side reactions. Therefore, we performed the further electrochemical measurements with an operation window between 0 and 1.5 V. As illustrated in Fig. 7c, the shape of the CV curves remains well-preserved with increasing scan rate, indicating a great rate capability for energy storage. The GCD profiles of this device tested at 1 A/g with different voltage windows are given in Fig. 7d. The discharge time increases significantly with the expansion of the operating voltage window from 1.2 to 1.5 V. Consequently, the specific capacitance of the NMO//NiO-9//AC device can be increased from 55 to 149.4 F/g, accompanied by a remarkable enhancement in energy density from 11 to 46.6 W h/kg (Fig. 7e). The GCD profiles and the corresponding specific capacitance for the device at current densities from 1 to 7 A/g are shown in Fig. 7f and 7g. The capacitance values are 149.4, 137.8, 130.1, 123.8, 118.0, 113.2 and 109.6 F/g at current densities of 1, 2, 3, 4, 5, 6 and 7 A/g, respectively. Fig. 7h presents the cycling stability of the device at current density of 5 A/g. Remarkably, after 5000 cycles, NMO/NiO-9//AC device demonstrates excellent cycling stability and shows around 81.6% of the specific capacitance retention. Finally, the overall performance of the NMO/NiO-9//AC device is examined by the Ragone plot as shown in Fig. 7i. The device can achieve a maximum energy density of 46.6 W h/kg at a power density of 750 W/kg. The obtained energy density can rival those values of previously reported NMO based asymmetric supercapacitors such as

$CoMoO_4$@$NiMoO_4$//AC (28.7 W h/kg) [37], $NiMoO_4$-PANI//AC (33.07 W h/kg) [38], 50-NiMo-HCNF//AC (30 W h/kg) [39], NMO-500//O,N-AC (64.07 W h/kg) [40], NiMo-7//AC (50.13 W h/kg) [35], NG/$NiMoO_4$//AC (22.2 W h/kg) [41], NF/$NiMoO_4$/$NiMoO_4$ (47.13 W h/kg) [42], OD-NF//AC (49.1 W h/kg) [43], $NiMoO_4$ NF//AC (39 W h/kg) [44], $NiMoO_4$@rGO/NF//AC (40 W h/kg) [45], $NiMoO_4$-rGO//NG (30.3 W h/kg) [46], NMC-2//AC (40.9 W h/kg) [47], $NiMoO_4$//$NiMoO_4$ (41.5 W h/kg) [48], $NiMoO_4$//NrGO/CNT (45.23 W h/kg) [49], $NiMoO_4$/rGO- 450/PPy//AC/graphite (43.65 W h/kg) [50].

3.3 The photocatalytic capability of NMO/NiO composite

In this study, the photocatalytic property of the NMO/NiO composite was also systematically explored. In general, the optical absorbance and surface area play crucial roles in photocatalytic processes, directly influencing the utilization of solar energy and the availability of sites for photocatalytic reactions with surrounding substances. The UV−vis diffuse reflectance spectra and the corresponding Tauc’s plots of these samples are shown in Fig. 8a and 7b. The Tauc’s plot of $(\alpha h\nu)^2$ vs. hν for these samples as shown in Fig. 8b can be used to evaluate the band gap energy (*E*g) by extrapolating the linear part of $(\alpha h\nu)^2$ equal to zero. As the pH value of the precursor solution increases, the obtained samples exhibit *E*g value of 3.07, 2.91, 2.65, 2.45, and 3.21 eV, respectively. In general, the *E*g value of the resultant product decreases with increasing the content of β-NMO, confirming that the β-NMO is more conductive phase than α-NMO [33, 34]. The N_2 adsorption-desorption isotherms of the five samples are shown in Fig. 8c. Based on the results, the NMO/NiO-9 exhibits the highest surface area among the samples. The surface areas of these samples, prepared at pH values ranging from 1 to 11, are 31.9, 47.5, 70.5, 144.0, and 100.8 m^2/g, respectively. According to the isotherm curve, the NMO/NiO-9 displays a type IV isotherm loop, indicating its mesoporous structure and its high surface area is favorable for supercapacitive and photocatalytic applications. The photocatalytic capability of these samples was evaluated by monitoring the degradation of MB under visible light irradiation. The degradation efficiency of NMO/NiO-3, NMO/NiO-5, NMO/NiO-7, NMO/NiO-9 within 160 min is found to be 51.3, 62.5, 70.0 and 82.3%, respectively. The degradation kinetics of the MB dye follows a pseudo-first-order reaction, described by the equation: $-\ln(C/C_0) = \underline{k}\times t$, where k is the photocatalytic reaction rate constant, C_0 is the initial concentration of MB, and C is the concentration of MB at the reaction time t. As shown in Fig. 8e, the NMO/NiO-9 reveals a much higher k value (0.0113 min^{-1}) than that of NMO/NiO-3, NMO/NiO-5, NMO/NiO-7 and NMO/NiO-11 (0.0044, 0.0062, 0.0075 and 0.0022 min^{-1}). The corresponding degradation absorption spectra of MB as a function of irradiation time in the presence of NMO/NiO-9 composite is also shown in Fig. 8f. The other four degradation absorption spectra of MB are also shown in Fig. S6. As shown in Fig. 8d and e, as the pH value is increased from 3 to 9, the photocatalytic activity of the resulting NMO/NiO composite gradually improves. This indicates that the β-NMO phase not only improves the supercapacitive performance but also has a positive impact on the photocatalytic degradation. However, with a further increase in pH value to 11, the degradation efficiency dramatically decreases to 29.1%, which is probably caused by the change in crystal structure from binary phase (MNO/NiO) to single NiO phase confirmed by the XRD results (Fig. 5a). The single NiO phase (pH=11) without the heterojunction reveals poor photocatalytic capability due to the severe charge recombination [51]. Similarly, the pure NMO phase also demonstrates very limited photocatalytic activity, with a low k value of 0.0018 min^{-1}. (Please see Fig. S7). The photocatalytic performance was further examined by measuring the transient photocurrent response. As shown in Fig. 8g, all the samples exhibit rapid and reproducible photoresponses under illumination. Additionally, the order of the photocurrent densities corresponds to the trend of rate constants as shown in Fig. 8e. The enhancement in photocatalytic capability of NMO/NiO-9 is mainly originated from the improved charge transfer and separation, facilitated by the highly conductive β-MNO phase and the construction of the NMO/NiO hierarchical heterojunction. In addition, the quenching tests by different scavengers were also carried out to identify the dominant active species involved in the photocatalytic degradation. Here, three typical scavengers, including isopropanol (IPA), benzoquinone (BQ), and ethylenediaminetetraacetic acid (EDTA) were used to quench $\bullet OH$, $\bullet O_2^-$, and h^+, respectively [52]. As shown in Fig. 8h, a dramatic decrease in degradation efficiency can be observed in the presence of IPA and BQ. However, the addition of EDTA cannot alter the photocatalytic performance of NMO/NiO-9.

These results clearly verify that the both $\bullet OH$ and $\bullet O_2^-$ play a predominant role in MB degradation. The durability of the binary NMO/NiO-9 composite was evaluated through repeated experiments for MB degradation, with the results displayed in Fig. 8i. After four cycles, the removal efficiency of NMO/NiO-9 only slightly decreases from 82.5% to 77.8%, indicating its excellent reusability.

The band structure of semiconductors is crucial for understanding the charge transfer and redox reactions in semiconductor photocatalysts. To explore the band structure of NMO/NiO-9, the UV−vis diffuse reflectance spectrum and Mott-Schottky (MS) measurement of pure NMO and NiO were investigated. The UV–Vis diffuse reflectance spectra of NMO and NiO are shown in Fig. 9a. It can be seen that the NMO demonstrates pronounced absorption in the visible light range (420–600 nm) and the absorption edge is approximately 550 nm. While the bare NiO exhibits strong absorption across the ultraviolet to visible light spectrum, with an absorption onset at approximately 370 nm. Moreover, the Eg value of NMO and NiO estimated through plot of $(\alpha h\nu)^2$ vs. hν as shown in Fig. 9b and 9c, is found to be 2.32 and 3.21 eV, respectively. To further determine the conduction (E_{CB}) and valence band edge potentials (E_{VB}) of NMO and NiO, the MS measurement was carried out. As shown in Fig. 9d and 9e, the MS plot of NMO shows a positive slope, indicating it is a n-type semiconductor, while NiO displays a negative slope, suggesting it is a p-type semiconductor. In addition, the MS plot of NMO/NiO-9 presented in Fig. 9f displays a reverse V-shape with two distinguish regions, confirming the successful construction of the p-n heterojunction between NMO and NiO [53]. Based on the MS plots, the flat-band potentials (E_{FB}) of NMO and NiO can be found to be 0.27 and 1.55 V (vs. Ag/AgCl), respectively, equivalent to 0.47 and 1.75 V (NHE). It is generally accepted that the E_{FB} of n-type semiconductors is approximately 0.2 V lower (more negative) than the E_{CB}, while for p-type semiconductors, the E_{FB} is about 0.2 V higher (more positive) than the E_{VB} [54-57]. Therefore, the E_{CB} of NMO and E_{VB} of NiO can be determined to be 0.27 and 1.95 V (NHE), respectively. Combined with the Eg values obtained from Fig. 9b and 9c, the E_{VB} of NMO and E_{CB} of NiO are 2.59 and -1.26 V (NHE), respectively. Based on the information regarding the E_{CB} and E_{VB}, the energy band structure of the pure NMO, NiO (left of Fig. 9g) and NMO/NiO composite (right of Fig. 9g) can be proposed. For the single component (both pure NMO and NiO), it is unfavorable for photocatalytic reaction due to the rapid charge recombination. In contrast, with the construction of NMO/NiO hierarchical heterojuntion, the charge separation can be facilitated through the direct Z-scheme heterojunction. Under light irradiation, the built-in electric field between the NMO and NiO interface can result in rapid recombination of the photoinduced electrons of NMO and the holes of NiO. The E_{CB} of NiO is higher than the reduction potential of dissolved oxygen (−0.33 eV vs. NHE) [58] and the E_{VB} of NMO is also lower than the H_2O/•OH redox potential (2.38 V vs. NHE) [59]. As a result, the holes left in E_{VB} of NMO and the electrons in E_{CB} of NiO can further react with H_2O and O_2 to produce •OH and $•O_2^-$ radicals, respectively which are the major active species for the photocatalytic process according to the trapping experiments (Fig. 8h). The Z-scheme NMO/NiO heterojunction can efficiently separate the photoinduced carriers leading to better photocatalytic capability than that of pure NiO.

4. Conclusion

In summary, the NMO/NiO hierarchical heterojunction applied for supercapacitor and photocatalyst has been prepared. By adjusting the post annealing temperature and the pH value of precursor solution, the ratio of α-phase to β-phase content in NMO can be regulated. The β-phase NMO reveals both better supercapacitive and photocatalytic performance that that of α-phase one attributed from its high conductivity and rapid charge transfer. The experimental results show that a high annealing temperature and an alkaline condition (pH=9) can promote the formation of the β-phase of MNO. The optimal NMO/NiO-9 (annealed at 600 ºC) demonstrates great electrochemical performance with a specific capacitance of 943 F/g at 1 A/g and retains 83.2% of this value at 6 A/g. The asymmetric device incorporated with NMO/NiO and AC also can deliver a high energy density of 46.6 W h/kg at a power density of 750 W h/kg. Furthermore, the NMO/NiO-9 heterojunction also exhibits significant photocatalytic activity for MB degradation. The degradation efficiency of NMO/NiO-9 is 3.14 and 2.83 times higher than that of pure NMO and NiO. The improved photocatalytic activity is originated from the built p-n heterojunction leading to the inhibition of photogenerated electron-hole recombination.

ACKNOWLEDGMENT

The financial support provided by Chang Gung University (URRPD2N0021) is gratefully appreciated.

REFERENCES

[1] J. Bhagwan, Sk. K. Hussain, J. S. Yu, Facile hydrothermal synthesis and electrochemical properties of $CaMoO_4$ nanoparticles for aqueous asymmetric supercapacitors, ACS Sustainable Chem. Eng. 7 (2019) 12340–12350.

[2] E. Figueroa-González, A. I. Oliva, V. Rodriguez-Gonzalez, C. Gomez-Solis, C. R. Garcia, J. Oliva, Using recycled tetrapak and Ag/$BaMoO_4$ nanoparticles to make efficient and flexible solid state supercapacitors, J. Energy Storage 47 (2022) 103544.

[3] M. Minakshi, D. R. G. Mitchell, A. R. Munnangi, A. J. Barlow, M. Fichtner, New insights into the electrochemistry of magnesium molybdate hierarchical architectures for high performance sodium devices, Nanoscale 10 (2018) 13277-13288.

[4] P. Sivakumar, L. Kulandaivel, J. W. Park, C. J. Raj, R. Ramesh, H. Jung, Rational design and fabrication of one-dimensional hollow cuboid-like $FeMoO_4$ architecture as a high performance electrode for hybrid supercapacitor, Ceram. Int. 48 (2022) 29144-29151.

[5] O. R. Ankinapalli, B. N. V. Krishna, R. R. Ayyaluri, J. S. Yu, $ZnMoO_4/MoO_3$ composite materials via facile one-step hydrothermal route for efficient hybrid supercapacitors, J. Energy Storage 85 (2024) 111043.

[6] D. Du, R. Lan, W. Xu, R. Beanland, H. Wang, S. Tao, Preparation of a hybrid $Cu_2O/CuMoO_4$ nanosheet electrode for high-performance asymmetric supercapacitors, J. Mater. Chem. A 4 (2016) 17749-17756.

[7] J. Bhagwan, Sk. K. Hussain, B. N. V. Krishna, J. S. Yu, Facile synthesis of $MnMoO_4$@MWCNT and their electrochemical performance in aqueous asymmetric supercapacitor, J. Alloys Compd. 856 (2021) 157874.

[8] L. Q. Mai, F. Yang, Y. L. Zhao, X. Xu, L. Xu, Y. Z. Luo, Hierarchical $MnMoO_4/CoMoO_4$ heterostructured nanowires with enhanced supercapacitor performance, Nat. Commun. 2 (2011) 381.

[9] S. Peng, L. Li, H. B. Wu, S. Madhavi, X. W. Lou, Controlled growth of $NiMoO_4$ nanosheet and nanorod arrays on various conductive substrates as advanced electrodes for asymmetric supercapacitors, Adv. Energy Mater. 5 (2015) 1401172.

[10] J. A. Rodriguez, S. Chaturvedi, J. C. Hanson, A. Albornoz, J. L. Brito, Electronic properties and phase transformations in $CoMoO_4$ and $NiMoO_4$: XANES and time-resolved synchrotron XRD studies, J. Phys. Chem. B 102 (1998) 1347-1355.

[11] T. Watcharatharapong, M. Minakshi Sundaram, S. Chakraborty, D. Li, G. M. Shafiullah, R. D. Aughterson, R. Ahuja, Effect of transition metal cations on stability enhancement for molybdate based hybrid supercapacitor, ACS Appl. Mater. Interfaces 9 (2017) 17977-17991.

[12] M. A. Ávila-López, E. Luévano-Hipólito, L. M. Torres-Martínez, Optimizing the CO2 reduction to produce CH_3OH using flexible $NiMoO_4$ coatings as a photocatalyst, J. Alloys Compd. 918 (2022) 165549.

[13] S. K. Ray, J. Hur, A critical review on modulation of $NiMoO_4$-based materials for photocatalytic applications, J. Environ. Manage. 278 (2021) 111562.

[14] L. Gurusamy, L. Karuppasamy, S. Anandan, C. H. Liu, J. J. Wu, Recent advances on metal molybdate-based electrode materials for supercapacitor application, J. Energy Storage 79 (2024) 110122.

[15] G. Sanyal, B. Mondal, C. S. Rout, B. Chakraborty, Recent developments and future perspectives on energy storage and conversion applications of nickel molybdates, Energy Storage 5 (2023) e432.

[16] S. K. Ray, J. Hur, A critical review on modulation of $NiMoO_4$-based materials for photocatalytic applications, J. Environ. Manage. 278 (2021) 111562.

[17] R. Liu, A. Zhou, X. Zhang, J. Mu, H. Che, Y. Wang, T. T. Wang, Z. Zhang, Z. Kou, Fundamentals, advances and challenges of transition metal compounds-based supercapacitors, J. Chem. Eng. 412 (2021) 128611.

[18] M. Cui, X. Meng, Overview of transition metal-based composite materials for supercapacitor electrodes, Nanoscale Adv. 2 (2020) 5516-5528.

[19] S. K. Ray, A. K. Reddy P, S. Yoon, J. Shin, K. Chon, S. Bae, A magnetically separable α-$NiMoO_4/ZnFe_2O_4$/coffee biochar heterojunction photocatalyst for efficient ketoprofen degradation, J. Chem. Eng. 452 (2023) 139546.

[20] Y. Ma, J. Xu, S. Xu, Z. Liu, X. Liu, Z. Li, Y. Shang, Q. Li, Construction of 3D/3D heterojunction between new noble metal free $ZnIn_2S_4$ and non-inert metal $NiMoO_4$ for enhanced hydrogen evolution performance under visible light, Int. J. Hydrogen Energy 48 (2023) 26707-26717.

[21] H. Ehrenberg, I. Svoboda, G. Wltschek, M. Wiesmann, F. Trouw, H. Weitzel, H. Fuess, Crystal and magnetic structure of α-$NiMoO_4$, J. Magn. Magn. Mater. 150 (1995) 371-376.

[22] C. Mazzocchia, C. Aboumrad, C. Diagne, E. Tempesti, J. M. Herrmann, G. Thomas, On the $NiMoO_4$ oxidative dehydrogenation of propane to propene: some physical correlations with the catalytic activity, Catal. Lett. 10 (1991) 181-191.

[23] M. El-Kemary, N. Nagy, I. El-Mehasseb, Nickel oxide nanoparticles: Synthesis and spectral studies of interactions with glucose, Mater. Sci. Semicond. Process. 16 (2013) 1747–1752.

[24] M. W. Alam, A. BaQais, T. A. Mir, I. Nahvi, N. Zaidi, A. Yasin, Effect of Mo doping in NiO nanoparticles for structural modification and its efficiency for antioxidant, antibacterial applications, Sci. Rep. 13 (2023) 1328.

[25] J. Yesuraj, O. Padmaraj, S. A. Suthanthiraraj, Synthesis, characterization, and improvement of supercapacitor properties of $NiMoO_4$ nanocrystals with polyaniline, J. Inorg. Organomet. Polym. 30 (2020) 310–321.

[26] O. Popovych, I. Budzulyak, V. Vashchynskyi, M. Khemii, R. Ilnytskyi, L. Yablon, Microwave-assisted synthesis of nanocrystalline $NiMoO_4$ for hybrid supercapacitor applications, Appl. Nanosci. 13 (2023) 6803–6809.

[27] P. Sharma, M. Minakshi, J. Whale, A. Jean-Fulcrand, G. Garnweitner, Effect of the anionic counterpart: Molybdate vs. tungstate in energy storage for pseudo-capacitor applications, 11 (2021) 580.

[28] S. S. Saleem, Infrared and Raman spectroscopic studies of the polymorphic forms of nickel, cobalt and ferric molybdates, Infrared Phys. 27 (1987) 309-315.

[29] H. M. Abdel-Dayem, Dynamic phenomena during reduction of α-$NiMoO_4$ in different atmospheres: In-situ thermo-Raman spectroscopy study, Ind. Eng. Chem. Res. 46 (2007) 2466–2472.

[30] R. Xu, J. Lin, J. Wu, M. Huang, L. Fan, Z. Xu, Z. Song, A high-performance pseudocapacitive electrode material for supercapacitors based on the unique $NiMoO_4/NiO$ nanoflowers, Appl. Surf. Sci. 463 (2019) 721-731.

[31] Q. Tang, M. Ye, L. Ma, T. Zhou, M. Gan, F. Yan, Facile synthesis of Ni–Mn layered double hydroxide nanopetals on 3D reduced graphene oxide/Ni foam for high-performance supercapacitors, Nano 15 (2020) 2050021.

[32] L. Huang, B. Liu, H. Hou, L. Wu, X. Zhu, J. Hu, J. Yang, Facile preparation of flower-like NiMn layered double hydroxide/reduced graphene oxide microsphere composite for high-performance asymmetric supercapacitors, J. Alloys Compd. 730 (2018) 71-80.

[33] D. Cai, D. Wang, B. Liu, Y. Wang, Y. Liu, L. Wang, H. Li, H. Huang, Q. Li, T. Wang, Comparison of the electrochemical performance of $NiMoO_4$ nanorods and hierarchical nanospheres for supercapacitor applications, ACS Appl. Mater. Interfaces 5 (2013) 12905−12910.

[34] B. Moreno, E. Chinarro, M. T. Colomer, J. R. Jurado, Combustion synthesis and electrical behavior of nanometric β-$NiMoO_4$, J. Phys. Chem. C 114 (2010) 4251–4257.

[35] R. Yang, X. Guo, K. Song, X. Bai, L. Jia, X. Chen, X. Wang, J. Wang, Influence of pH on the crystal structure of $NiMoO_4$ nanomaterials and their supercapacitor performances, Ceram. Int. 47 (2021) 11349–11357.

[36] G. Zha, N. Hu, Y. Luo, F. Wang, R. Wu, Y. Li, H. Fu, X. Fu, Reducing Ni/Li disorder and boosting electrochemical performance of $LiNi_{0.8}Co_{0.067}Fe_{0.033}Mn_{0.1}O_2$ cathode material, J. Taiwan Inst. Chem. Eng. 144 (2023) 104730.

[37] Z. Zhang, H. Zhang, X. Zhang, D. Yu, Y. Ji, Q. Sun, Y. Wang, X. Liu, Facile Synthesis of hierarchical $CoMoO_4$@$NiMoO_4$ core-shell nanosheet arrays on nickel foam as an advanced electrode for asymmetric supercapacitors, J. Mater. Chem. A 4 (2016) 18578-18584.

[38] H. Gao, F. Wu, X. Wang, C. Hao, C. Ge, Preparation of $NiMoO_4$-PANI core-shell nanocomposite for the high-performance all-solid-state asymmetric supercapacitor, Int. J. Hydrogen Energy 43 (2018) 18349-18362.

[39] V. S. Budhiraju, R. Kumar, A. Sharma, S. Sivakumar, Structurally stable hollow mesoporous graphitized carbon nanofibers embedded with $NiMoO_4$ nanoparticles for high performance asymmetric supercapacitors, Electrochim. Acta 238 (2017) 337-348.

[40] C. J. Raj, R. Manikandan, K. H. Yu, G. Nagaraju, M. S. Park, D. W. Kim, S. Y. Park, B. C. Kim, Engineering thermally activated $NiMoO_4$ nanoflowers and biowaste derived activated carbon-based electrodes for high-performance supercapatteries, Inorg. Chem. Front. 7 (2020) 369-384.

[41] X. Feng, J. Ning, D. Wang, J. Zhang, M. Xia, Y. Wang, Y. Hao, Heterostructure arrays of $NiMoO_4$ nanoflakes on N-doping of graphene for highperformance asymmetric supercapacitors, J. Alloys Compd. 816 (2020) 152625.

[42] A. K. Yedluri, T. Anitha, H. J. Kim, Fabrication of hierarchical $NiMoO_4$/$NiMoO_4$ nanoflowers on highly conductive flexible nickel foam substrate as a capacitive electrode material for supercapacitors with enhanced electrochemical performance, energies 12 (2019) 1143.

[43] C. Qing, C. Yang, M. Chen, W. Li, S. Wang, Y. Tang, Design of oxygen-deficient $NiMoO_4$ nanoflake and nanorod arrays with enhanced supercapacitive performance, Chem. Eng. J. 354 (2018) 182-190.

[44] V. S. Budhiraju, A. Sharma, S. Sivakumar, Structurally stable mesoporous hierarchical $NiMoO_4$ hollow nanofibers for asymmetric supercapacitors with enhanced capacity and improved cycling stability, ChemElectroChem 4 (2017) 3331-3339.

[45] Y. Xu, H. Xuan, J. Gao, T. Liang, X. Han, J. Yang, Y. Zhang, H. Li, P. Han, Y. Du, Hierarchical three-dimensional $NiMoO_4$-anchored rGO/Ni foam as advanced electrode material with improved supercapacitor performance, J. Mater. Sci. 53 (2018) 8483–8498.

[46] T. Liu, H. Chai, D. Jia, Y. Su, T. Wang, W. Zhou, Rapid microwave-assisted synthesis of mesoporous $NiMoO_4$ nanorod/reduced graphene oxide composites for high-performance supercapacitors, Electrochim. Acta 180 (2015) 998-1006.

[47] K. Yousefipour, R. Sarraf-Mamoory, A. C. Maleki, A new strategy for the preparation of multi-walled carbon nanotubes/$NiMoO_4$ nanostructures for high-performance asymmetric supercapacitors, J. Energy Storage 59 (2023) 106438.

[48] X. Tian, T. Yang, Y. Song, Y. Li, H. Peng, R. Xue, X. Ren, Z. Liu, Symmetric supercapacitor operating at 1.5 V with combination of nanosheet-based $NiMoO_4$ microspheres and redox additive electrolyte, J. Energy Storage 47 (2022) 103960.

[49] M. S. Iyer, I. Rajangam, Hybrid nanostructures made of porous binary transition metal oxides for high performance asymmetric supercapacitor application, J. Energy Storage 67 (2023) 107530.

[50] R. Ghanbari, S. R. Ghorbani, High-performance nickel molybdate/reduce graphene oxide/polypyrrole ternary nanocomposite as flexible all-solid-state asymmetric supercapacitor, J. Energy Storage 60 (2023) 106670.

[51] X. Hua, G. Wang, J. Wang, Z. Hu, Y. Su, Step-scheme NiO/BiOI heterojunction photocatalyst for rhodamine photodegradation, Appl. Surf. Sci. 511 (2020) 145499.

[52] X. Yan, X. Yuan, J. Wang, Q. Wang, C. Zhou, D. Wang, H. Tang, J. Pan, X. Cheng, Construction of novel ternary dual Z-scheme Ag_3VO_4/C_3N_4/reduced TiO_2 composite with excellent visible-light photodegradation activity, J. Mater. Res. 34 (2019) 2024–2036.

[53] J. Y. Tang, C. C. Er, X. Y. Kong, B. J. Ng, Y. H. Chew, L. L. Tan, A. R. Mohamed, S. P. Chai, Two-dimensional interface engineering of g-C_3N_4/g-C_3N_4 nanohybrid: Synergy between isotype and p-n heterojunctions for highly efficient photocatalytic CO_2 reduction, Chem. Eng. J. 466 (2023) 143287.

[54] X. Tu, S. Qian, L. Chen, L. Qu, The influence of Sn(II) doping on the photoinduced charge and photocatalytic properties of BiOBr microspheres, J. Mater. Sci. 50 (2015) 4312–4323.

[55] D. S. Bhachu, S. J. A. Moniz, S. Sathasivam, D. O. Scanlon, A. Walsh, S. M. Bawaked, M. Mokhtar, A. Y. Obaid, I. P. Parkin, J. Tang, C. J. Carmalt, Bismuth oxyhalides: synthesis, structure and photoelectrochemical activity, Chem. Sci. 7 (2016) 4832-4841.

[56] Y. Wang, Y. Liang, D. Zeng, M. Zhu, J. Fu, T. Zhu, H. Han, C. Li, W. Wang, Electrochemical deposition of p-type β-$Ni(OH)_2$ nanosheets onto CdS nanorod array photoanode for enhanced photoelectrochemical water splitting, Electrochim. Acta 337 (2020) 135763.

[57] I. Vamvasakis, I.T. Papadas, T. Tzanoudakis, C. Drivas, S.A. Choulis, S. Kennou, G.S. Armatas, Visible-light photocatalytic H_2 production activity of β-$Ni(OH)_2$-modified CdS mesoporous nanoheterojunction networks, ACS Catal. 8 (2018) 8726-8738.

[58] R. Yang, Q. Zhao, B. Liu, Two-step method to prepare the direct Z-scheme heterojunction hierarchical flower-like Ag@AgBr/Bi2MoO6 microsphere photocatalysts for waste water treatment under visible light, J. Mater. Sci. Mater. Electron 31 (2020) 5054–5067.

[59] L. Luo, T. Zhang, M. Wang, R. Yun, X. Xiang, Recent advances in heterogeneous photo-driven oxidation of organic molecules by reactive oxygen species, ChemSusChem 13(2020) 5173-5184.

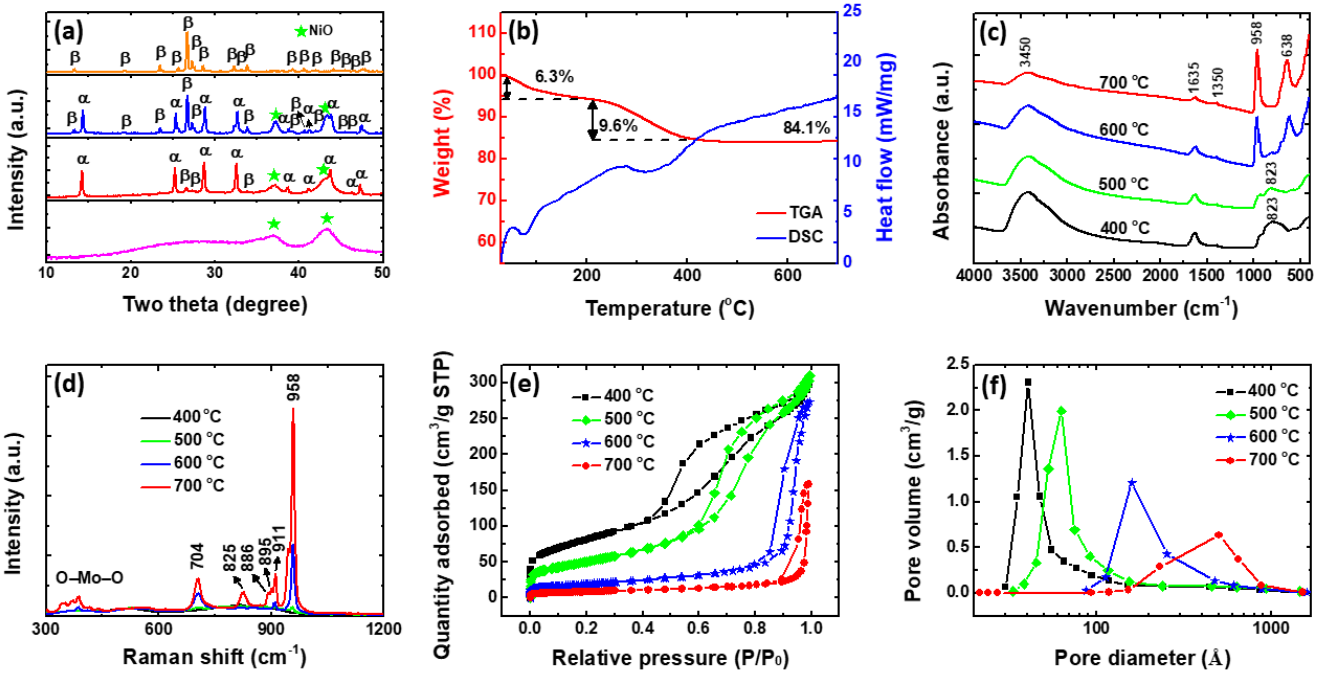

Figure. 1 The characterization of the NMO/NiO composites. (a) XRD pattern; (b) TGA/DSC curve; (c) FTIR spectrum; (d) Raman spectrum; (e) N_2 adsorption/desorption isotherms and (f) the the corresponding pore size distribution of the NMO/NiO composites annealed at different temperatures.

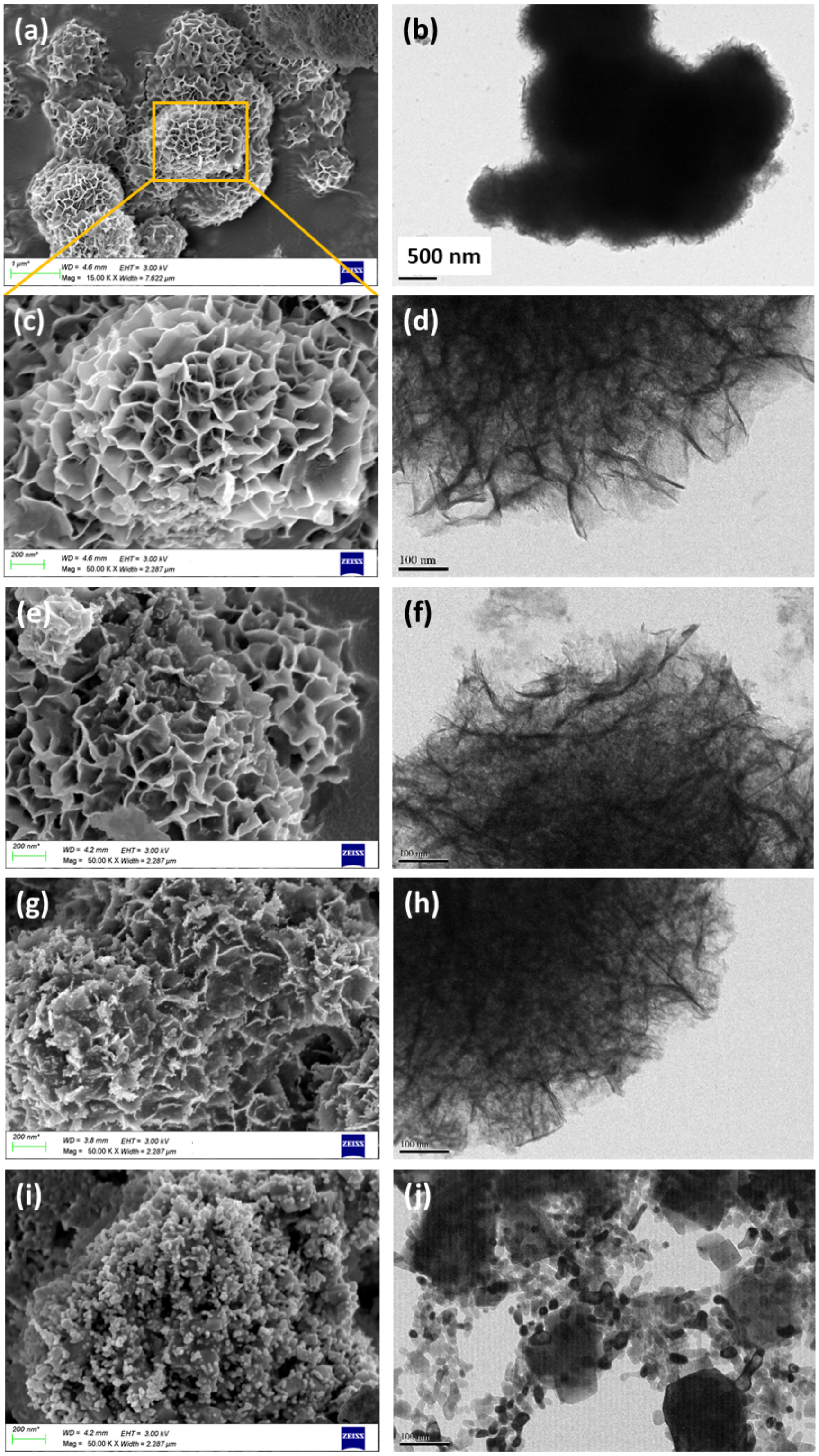

Figure 2. The morphology of the as-prepared samples with various annealing temperatures. The SEM images of the samples annealed at (a, c) 400 °C; (e) 500 °C ; (g) 600 °C and (i) 700 °C; the TEM image of the samples annealed at (b, d) 400 °C; (f) 500 °C; (h) 600 °C and (j) 700 °C.

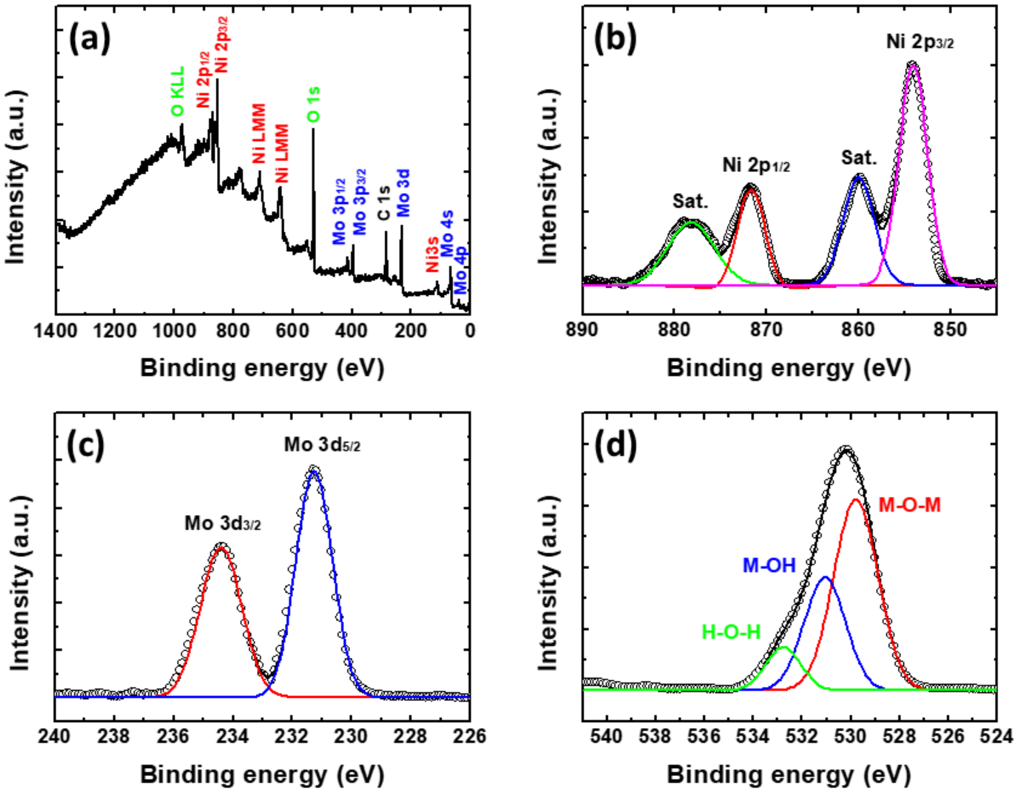

Figure 3. The investigation of chemical composition and state of the NMO/CMO composite. (a) XPS survey of the NMO/NiO composite annealed at 600 °C; (b) the peak deconvolution of the Ni 2p; (c) Mo 3d and (d) O 1s XPS spectrum of the NMO/CMO composite annealed at 600 °C.

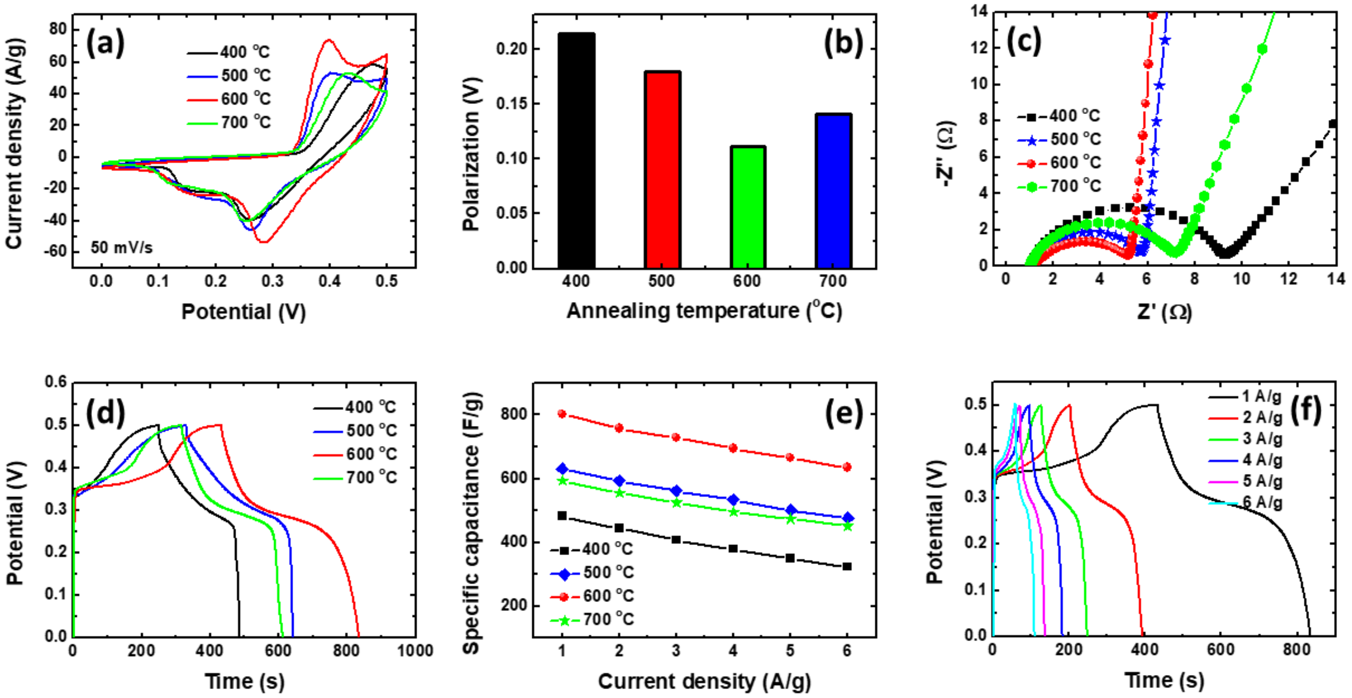

Figure 4. The effect of annealing temperature on the electrochemical property. (a) CV profiles (scan rate: 50 mV/s); (b) electrochemical polarization; (c) Nyquist plots; (d) GCD profiles; (e) rate performance of the as-prepared samples annealed at different temperatures and (f) the corresponding GCD profiles of the sample annealed at 600 ^{o}C.

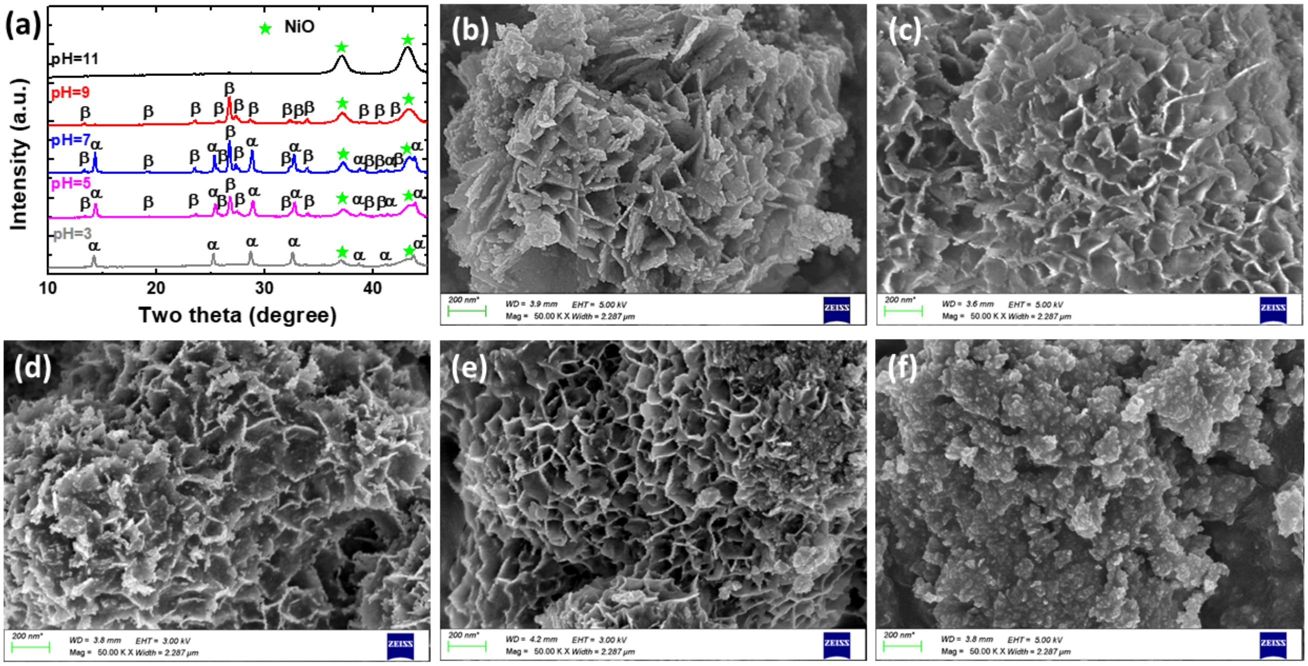

Figure 5. The structural and morphological evolution of NMO/NiO with different pH values. (a) XRD pattern of the NMO/NiO prepared with different pH value (annealed at 600 ºC); the SEM image of the samples prepared with (b) pH=3; (c) pH=5; (d) pH=7; (e) pH=9 and (f) pH=11.

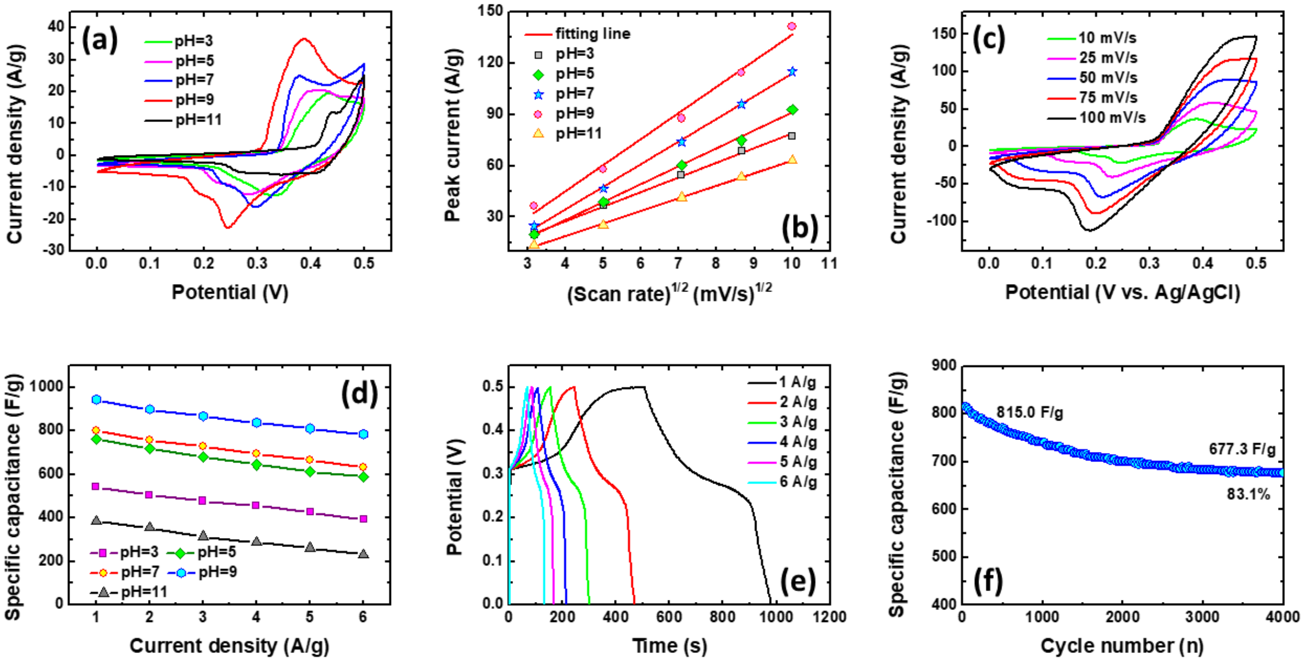

Figure 6. The effect of pH value on electrochemical property. (a) CV profiles and (b) the linear relationship of the anodic peak current (*i*) and the square root of scan rate ($\upsilon^{1/2}$) of the samples prepared from different pH values; (c) CV profiles of NMO/NiO-9 with various scan rates; (d) rate performance of the samples prepared from different pH values; (e) GCD profiles of NMO/NiO-9 at different current densities and (f) cycling stability of NMO/NiO-9 tested at 5 A/g.

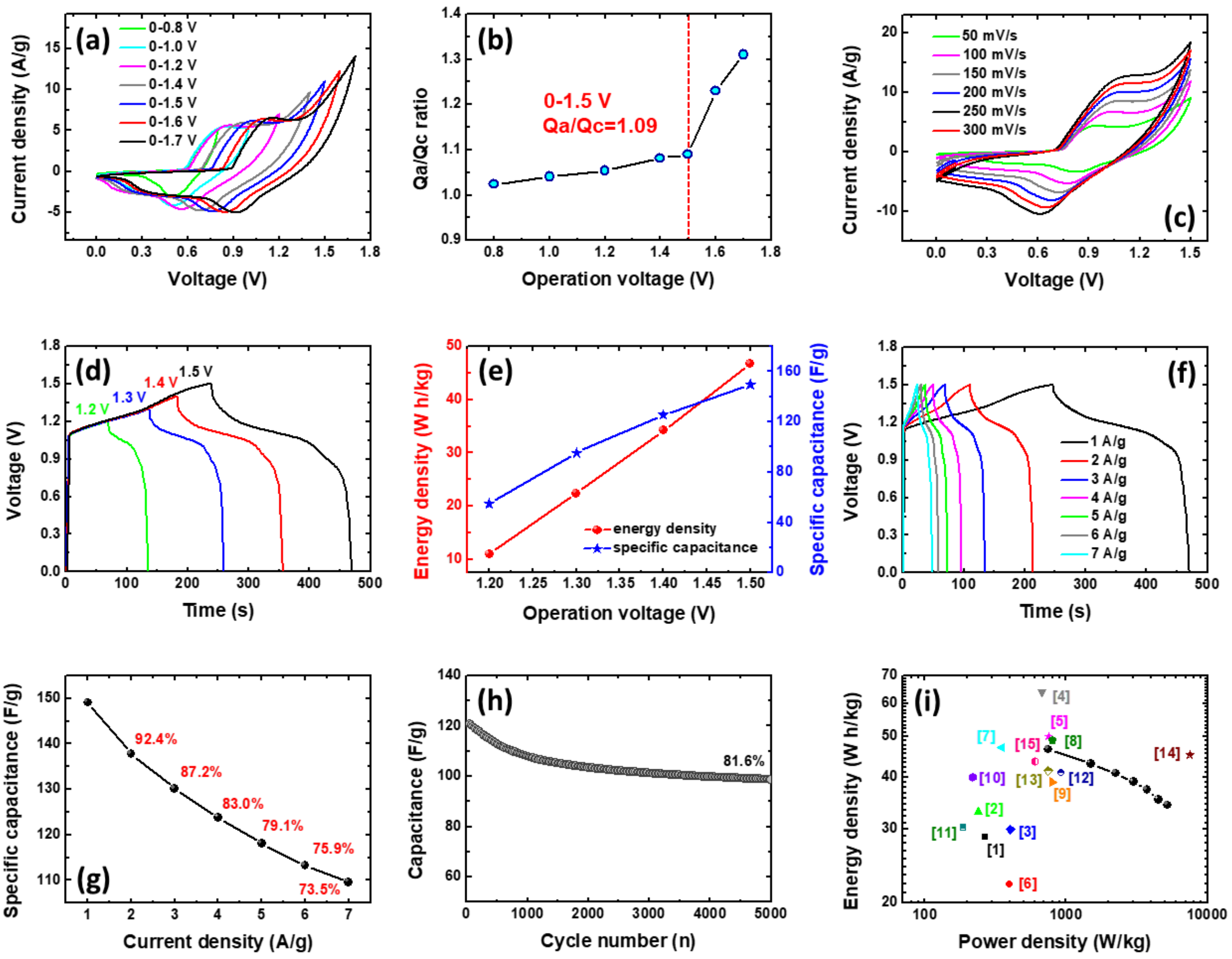

Figure 7. The energy storage performance of NMO/NiO-9//AC device. (a) CVs of the NMO/NiO-9//AC device at various operation windows at 100 mV/s; (b) ratio of the anodic to cathodic area (Qa/Qc) from the CV loop with different operation voltages; (c) CV curves at various scan rates; (d) GCD profiles of the NMO/NiO-9//AC device with different voltage windows; (e) energy density and specific capacitance of the device with the increase in the operation window at a fixed current density of 1 A/g; (f) GCD profiles of the NMO/NiO-9//AC device with various current densities; (g) rate performance; (h) cycling performance and (i) Ragone plot of the asymmetric supercapacitor compared with other reported data.

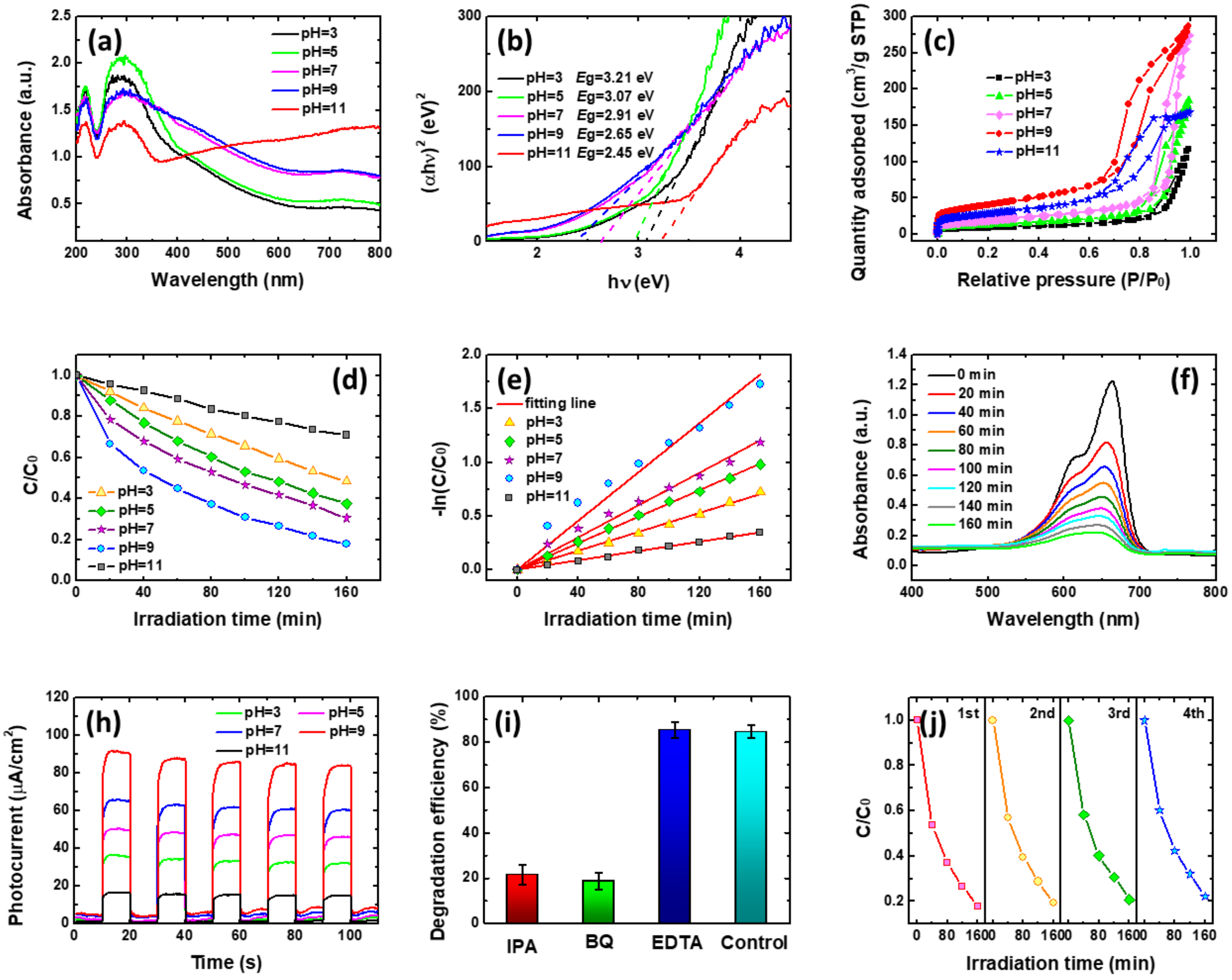

Figure 8. Photocatalytic performance of the NMO/NiO composite. (a) UV–Vis diffuse reflectance spectra and (b) the corresponding Tauc's plots; (c) N_2 adsorption/desorption isotherms; (d) photocatalytic degradation curves of MB and (e) the corresponding $-\ln(C/C_0)$–t plots of the samples prepared from different pH values; (f) UV–visible absorption spectra of MB solutions after being irradiated with visible light for different time in the presence of NMO/NiO-9 composite; (h) photocurrent of the five samples under illumination with visible light; (i) the effect of scavengers on the degradation process and (j) recycling runs of the NMO/NiO-9 heterojunction.

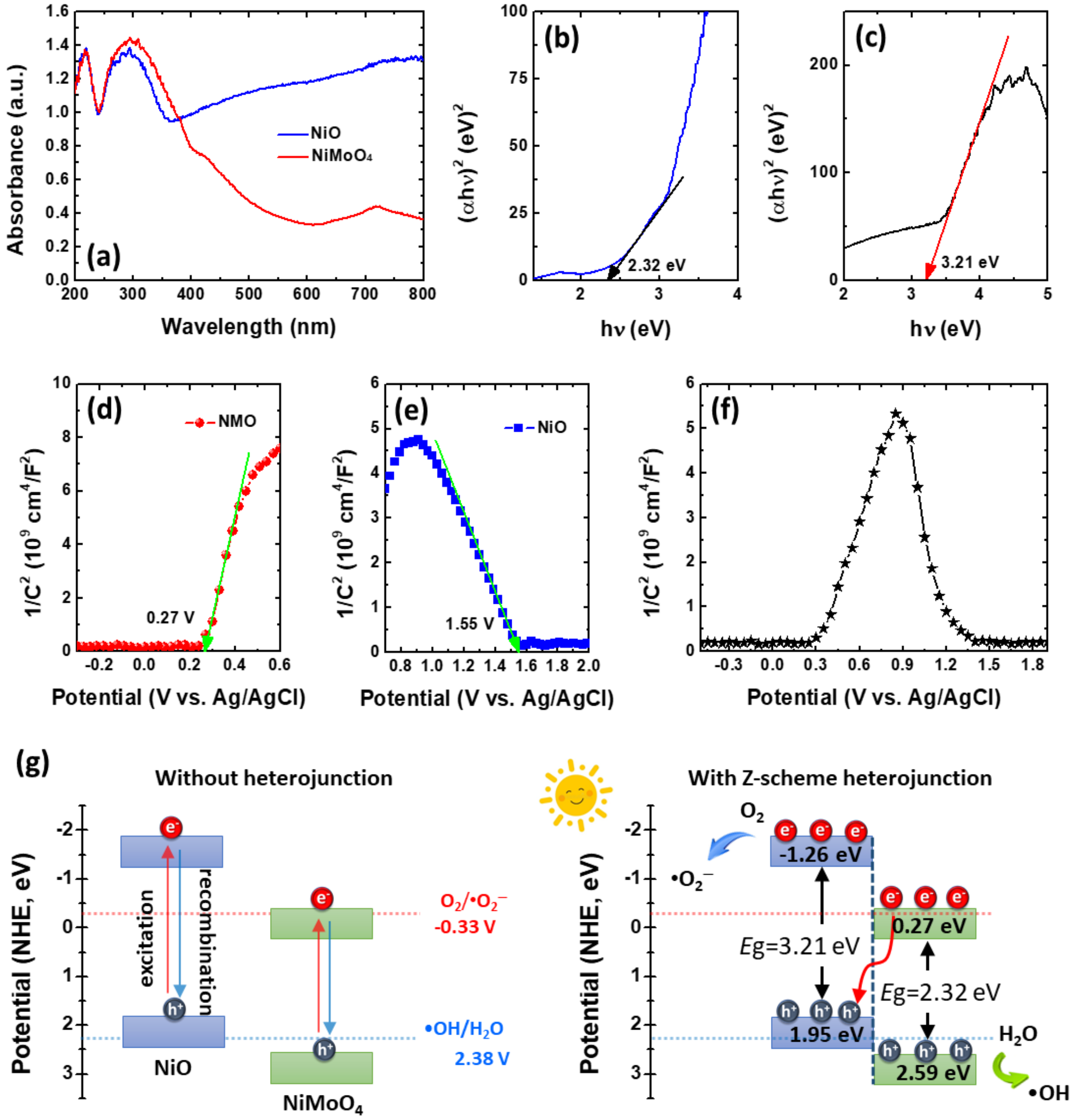

Figure 9. Band energy alignments between NMO and NiO. (a) UV–Vis diffuse reflectance spectra of NMO and NiO; the plots of $(\alpha h\nu)^2$ vs. hν for (b) NMO and (c) NiO; Mott–Schottky plots of (d) NMO, (e) NiO and (f) NMO/NiO-9; (g) mechanism scheme of photoexcited electron–hole pairs' separation process (left: single photocatalyst and right: Z direct scheme heterojunction).